
RS-vHEAT: HEAT CONDUCTION GUIDED EFFICIENT REMOTE SENSING FOUNDATION MODEL

A PREPRINT

Huiyang Hu^{1,2,3,4}, Peijin Wang^{1,2,3,4}, Hanbo Bi^{1,2,3,4}, Boyuan Tong^{1,2,3,4}, Zhaozhi Wang^{5,6}, Wenhui Diao^{1,2,3,4}, Hao Chang^{1,2,3,4}, Yingchao Feng^{1,2,3,4}, Ziqi Zhang⁷, Yaowei Wang^{5,7}, Qixiang Ye^{5,6}, Kun Fu^{1,2,3,4}, and Xian Sun^{1,2,3,4}

¹Aerospace Information Research Institute, Chinese Academy of Sciences

²School of Electronic, Electrical and Communication Engineering, University of Chinese Academy of Sciences

³University of Chinese Academy of Sciences

⁴Key Laboratory of Target Cognition and Application Technology

⁵Peng Cheng Laboratory

⁶School of Electronic, Electrical and Communication Engineering, University of Chinese Academy of Sciences

⁷State Key Laboratory of Multimodal Artificial Intelligence Systems, Institute of Automation, Chinese Academy of Sciences

⁸Harbin Institute of Technology (Shenzhen)

ABSTRACT

Remote sensing foundation models largely break away from the traditional paradigm of designing task-specific models, offering greater scalability across multiple tasks. However, they face challenges such as low computational efficiency and limited interpretability, especially when dealing with large-scale remote sensing images. To overcome these, we draw inspiration from heat conduction, a physical process modeling local heat diffusion. Building on this idea, we are the first to explore the potential of using the parallel computing model of heat conduction to simulate the local region correlations in high-resolution remote sensing images, and introduce RS-vHeat, an efficient multi-modal remote sensing foundation model. Specifically, RS-vHeat 1) applies the Heat Conduction Operator (HCO) with a complexity of $O(N^{1.5})$ and a global receptive field, reducing computational overhead while capturing remote sensing object structure information to guide heat diffusion; 2) learns the frequency distribution representations of various scenes through a self-supervised strategy based on frequency domain hierarchical masking and multi-domain reconstruction; 3) significantly improves efficiency and performance over state-of-the-art techniques across 4 tasks and 10 datasets. Compared to attention-based remote sensing foundation models, we reduce memory usage by 84%, FLOPs by 24% and improves throughput by 2.7 times. The code will be made publicly available.

Keywords Remote sensing foundation model · Self-supervised learning · Heat conduction · Remote sensing

1 Introduction

Recently, remote sensing (RS) technology has become a vital data source for scientific research, resource management, and environmental monitoring Sherrah [2016], Zhang et al. [2021], Sun et al. [2022a], Li et al. [2020a] by capturing surface information via satellites. Traditional models, designed as single-task networks for specific RS tasks Lu et al. [2021], Sun et al. [2021], struggle with multi-payload, multi-resolution, multi-temporal, and multi-feature RS data FU et al. [2021]. However, the emergence of remote sensing foundation models (RSFMs) has overcome these limitations, enabling unified handling of multiple tasks and diverse scenarios, significantly enhancing the scalability and versatility of the models Li et al. [2021], Manas et al. [2021], Mall et al. [2023], Ayush et al. [2021], Cong et al. [2022], Wang et al. [2022a], Tao et al. [2023], Reed et al. [2023], Mendieta et al. [2023], Bastani et al. [2023]. By constructing visual encoders, RSFMs can automatically extract and learn features from remote sensing imagery (RSI), providing a robust foundation for various real-world RS tasks.

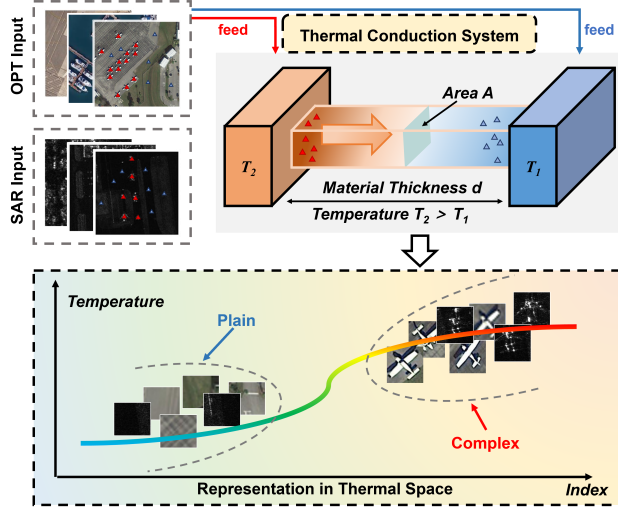


Figure 1: Calculation of RS images in the heat conduction system. In heat conduction theory, different materials exhibit varying diffusion rates. Inspired by this, the heat-conduction-based encoder maps optical (OPT) and synthetic aperture radar (SAR) into a unified thermal space, enhancing sensitivity to shape features by simulating heat flow and accumulation within the object region.

Prior RSFMs typically use visual encoders and decoders, leveraging large-scale RS datasets for pre-training while incorporating self-supervised learning strategies. Specifically, RSFMs can be categorized based on the type of backbone used: CNN-based methods often use ResNet18/50 He et al. [2016] to extract features Li et al. [2021], Manas et al. [2021], Mall et al. [2023], Ayush et al. [2021], while attention-based methods mainly use ViT Dosovitskiy et al. [2020] or Swin transformer Liu et al. [2021] with attention mechanisms Vaswani et al. [2017] to capture global dependencies Cong et al. [2022], Wang et al. [2022a], Tao et al. [2023], Reed et al. [2023], Mendieta et al. [2023], Bastani et al. [2023]. Both approaches use strategies such as masked reconstruction, knowledge distillation, or contrastive learning during pre-training to enhance model robustness (a detailed comparison is available in the supplementary materials). Despite the significant advancements achieved by these RSFMs, they still face two limitations:

Balancing Efficiency and Receptive Field. To accurately capture information about the large objects in RSI, model outputs must be responsive to sufficiently large regions Luo et al. [2016]. However, this need significantly increases computational complexity Christophe et al. [2011], Ma et al. [2015]. CNN-based networks lack a global receptive field due to their reliance on sliding computations with fixed-size convolutional kernels. While attention-based models achieve global modeling, their attention mechanisms incur quadratic computational complexity. Therefore, existing RSFMs struggle to deliver both fast and high-accuracy inference in practical applications.

Weak Physical Interpretability. RS objects often exhibit irregular polygonal shapes Li and Narayanan [2003], and current RSFMs struggle to integrate physical principles to explain how object features propagate. This deficiency makes it challenging for researchers to adjust learning strategies effectively Shen et al. [2022], Temenos et al. [2023], Pérez-Suay et al. [2020]. In the long term, RSFMs need to possess a certain degree of information interpretability.

To address these, this paper introduces RS-vHeat, a heat-conduction-based RSFM that supports multi-modal inputs inspired by the idea of vHeat Wang et al. [2024a]. **First**, heat conduction represents the natural process of energy diffusion from high- to low-temperature regions, as shown in the conceptual physical model in fig. 1. This process transitions from an unsteady to a steady state based on the material. Since its computational process resembles feature extraction in neural networks, it can be applied to RS image processing. **Second**, we hypothesize that object types correspond to special feature distributions, with the model predicting diffusion rates based on RS-specific properties, simulating parameter computation through heat flow. This approach projects all modalities into a common thermal space, following the constraint that complex areas containing RS objects are high-temperature regions where heat accumulates, while sparse regions are low-temperature areas where heat diffuses easily, as shown in the lower part of fig. 1. **Third**, building on this theory, we further design a RSFM with physical interpretability using 3 million optical and SAR data for pre-training, as shown in fig. 2. The heat conduction network simulates the diffusion process of heat across large-scale multi-modal RS data, facilitating the alignment of feature propagation with the structural characteristics of the objects. Moreover, its computational approach provides guidance for the efficient operation of the network.

To summarize, our contributions are as follows:

1. We introduce RS-vHeat, a RSFM designed based on the heat conduction differential equation to process RS data. It conceptualizes the semantic relationships between pixels in RS images as the propagation of heat.
2. We propose a self-supervised strategy based on frequency domain hierarchical masking and multi-domain reconstruction that preserves small objects, driving the model to reconstruct fine and coarse frequency signals.
3. We design spatial correction embeddings, which operate directly on the global features to capture local details, assisting in simulating the rate of thermal diffusion.
4. We evaluate RS-vHeat on 10 datasets, showing it outperforms advanced RSFMs in accuracy while maintaining lower computational complexity. When processing large-scale images, RS-vHeat reduces memory usage by 84%, decreases FLOPs by 24%, and improves throughput by 2.7 times compared to attention-based RSFMs.

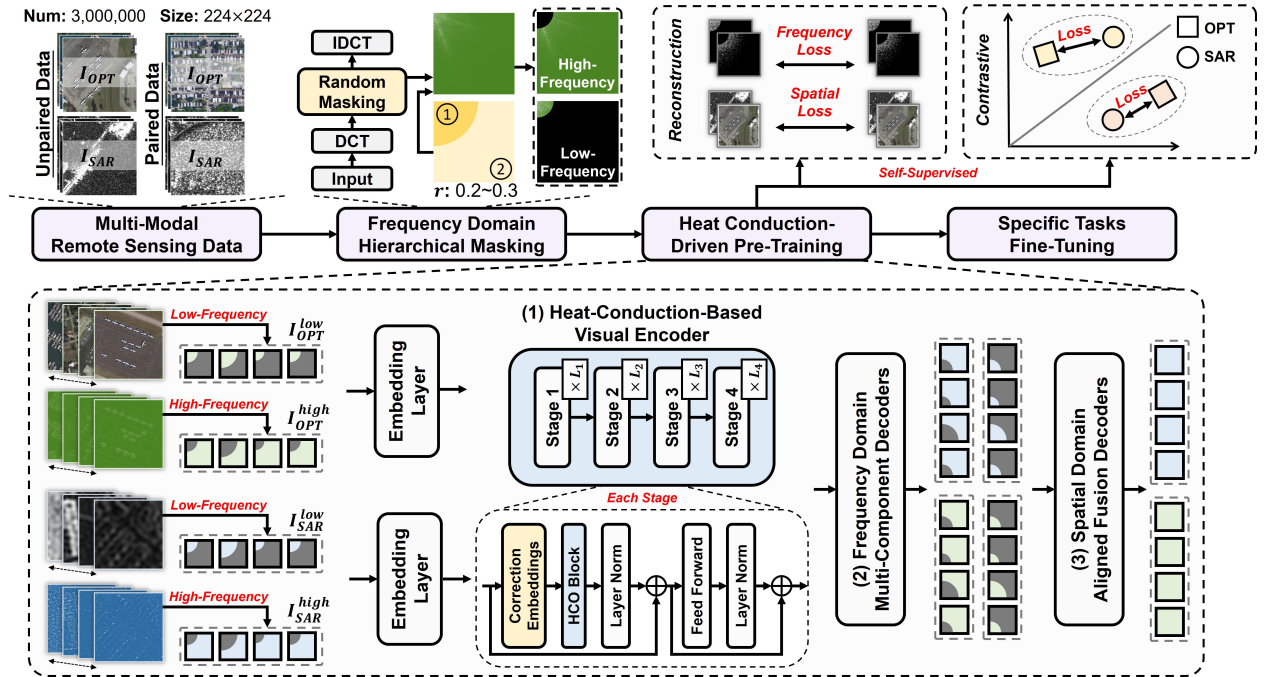


Figure 2: The pre-training process of RS-vHeat. It performs frequency domain hierarchical masking based on randomly generated sector regions to separate each image into high- and low-frequency components. These component images are fed into the network and projected into the thermal space via embedding layers. The heat diffusion is computed within the heat-conduction-based visual encoder to simulate complex RS objects. The deep features undergo multi-domain reconstruction loss and contrastive loss computation via decoders.

2 Related Work

2.1 Mainstream Network Architectures in RS

Convolutional Neural Networks. CNNs have been adapted for RS to tackle challenges in satellite imagery Zhang et al. [2019], Li et al. [2020b]. However, local receptive fields, mainly limited by the kernel size, restrict the capture of long-range dependencies Dosovitskiy et al. [2020]. This drawback is especially critical in RS, where large-scale patterns and complex spatial relationships are prevalent, making the balance between local feature extraction and global context a key research focus Dong et al. [2021], Chen et al. [2020].

Transformers. Self-attention mechanisms Vaswani et al. [2017] empower networks to capture long-range dependencies Dosovitskiy et al. [2020], Liu et al. [2021]. Research studies have shown that plain ViTs performs better than traditional CNN models in RS applications Wang et al. [2022a], Yan et al. [2022]. However, the limitation stems from the ViTs' restricted ability to effectively handle long sequences. When processing large-scale RS images, the computational load of networks grows quadratically, leading to significant overhead.

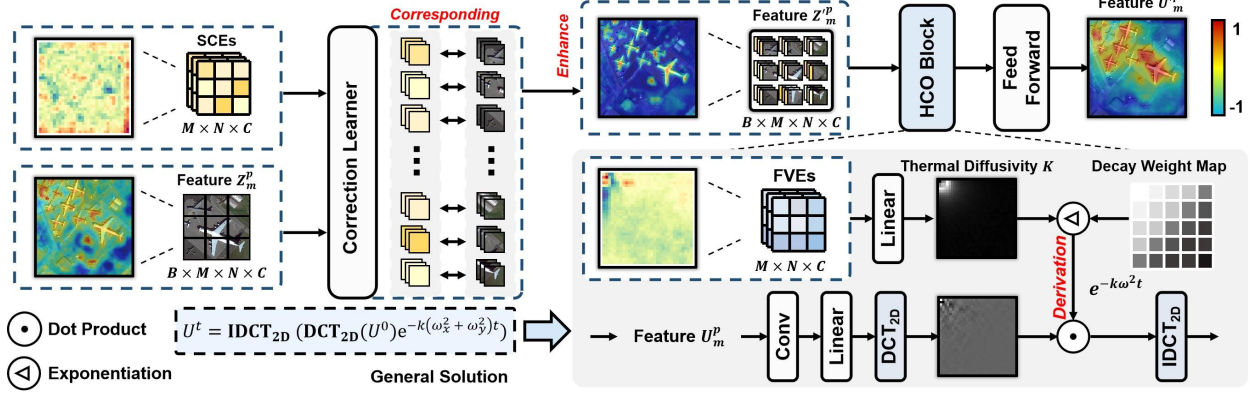


Figure 3: The overall structure of the heat-conduction-based visual encoder, simulates the general solution of heat conduction. SCEs first dynamically perform spatial domain correction, adjusting heat distribution based on the RS scene. The enhanced image undergoes a 2D DCT in the HCO block, interacting with the heat diffusion rate predicted by the FVEs to complete a heat conduction calculation, which is then transformed back into a visual representation via 2D IDCT.

Mamba-Based Models. Mamba, an efficient implementation of State Space Models (SSMs) Gu et al. [2021], leverages selective scan mechanisms for long-sequence processing Liu et al. [2024a], Zhu et al. [2024a], balancing computational efficiency and high accuracy. Gu and Dao [2023], Xu et al. [2024]. It has been rapidly adopted in RS Chen et al. [2024a], Zhu et al. [2024b], Chen et al. [2024b], with its ability to process long sequences, although Mamba, as an innovative architecture, suffers from limited interpretability.

2.2 Self-Supervised Learning Strategies for RSFMs

Contrastive Learning. By establishing rules to distinguish between positive and negative samples, contrastive learning aims to fully understand the relationships between these samples. GASSL Ayush et al. [2021] treats RS images of the same scene captured at different times as positive pairs, using them as self-supervised signals. Based on seasonal contrast method, SeCo Manas et al. [2021] and CACo Mall et al. [2023] effectively leverage temporal information within the networks by comparing scene variations across different years or seasons as perceptual signals. Skysense Guo et al. [2024] utilizes multi-modal RS images as input and implements a multi-granularity contrastive learning framework. Motivated by the aforementioned methods, we apply contrastive constraints in the thermal space to optical and SAR data, encouraging the model to focus on deep, fine-grained semantic relationships within the RS images.

Masked Image Modeling. By involving masking parts of the image and predicting the missing information, networks can understand the details of RSI. RingMo Sun et al. [2022b] attempts to solve the issue that directly masking image patches can easily lead to the loss of small objects by designing an incomplete masking strategy that is implemented proportionally within the patches. SpectralGPT Hong et al. [2024] models multi-spectral data as three-dimensional data and applies masking in three-dimensional space. Scale-MAE Reed et al. [2023] masks pixels in the spatial domain and reconstructs high- and low-frequency images to learn image representations at different scales. Inspired by these, to preserve and learn the information of complex RS scenes, we employ dual reconstruction in both the spatial and frequency domains as constraints.

3 Proposed RS-vHeat

We introduce RS-vHeat, a multi-modal remote sensing foundation model with three key components: a frequency domain hierarchical masking strategy for multi-modal RS data, a visual encoder for modeling internal heat flow within RS images, and decoders for multi-domain reconstruction. fig. 2 illustrates the RS-vHeat structure during pre-training, enabling shared representation of multi-modal data through frequency domain masking and projection into a thermal space to simulate heat propagation. Preliminary details on vHeat Wang et al. [2024a] are included in the supplementary materials.

Frequency Domain Hierarchical Masking Strategy. Traditional spatial masking Xie et al. [2022] on RS images often obscures smaller objects, hindering reconstruction. Inspired by the frequency-aware dynamic network Xie et al.

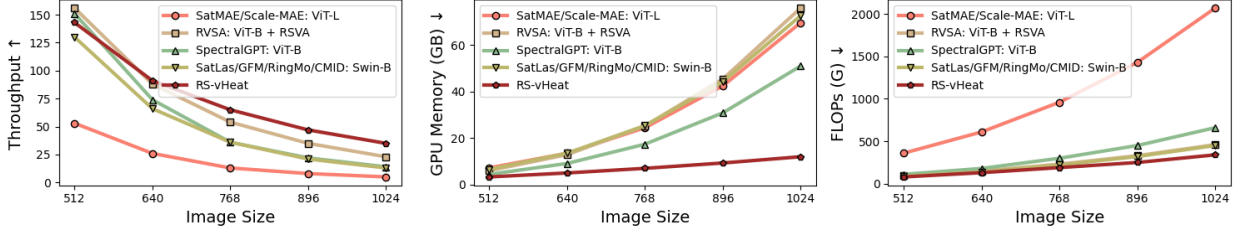


Figure 4: Comparison of throughput (left), GPU memory (middle), and FLOPs (right) across image sizes for RSFMs. RS-vHeat shows significantly higher throughput, lower memory usage and lower FLOPs than current attention-based RSFMs, especially for large-scale images. All tests were performed in a consistent environment using a single A100 (80G) GPU with a batch size of 32.

[2021a], we implement a frequency domain hierarchical masking strategy to preserve object structure, enabling more accurate heat propagation by focusing on frequency domain signals.

Specifically, given the input (optical and SAR), denoted as $I(x, y, c) = \{I_o, I_s\}$, $I_o \in \mathbb{R}^{H \times W \times 3}$, $I_s \in \mathbb{R}^{H \times W \times 1}$, two parallel streams process paired and unpaired data. The Discrete Cosine Transform (DCT) is applied along each image dimension, converting $I(x, y)$ to its frequency representation $\tilde{I}(u, v)$, where low-frequency components are concentrated in the top-left of the spectrum. A sector mask separates high-frequency $\tilde{I}^{high}(u, v)$ and low-frequency $\tilde{I}^{low}(u, v)$ regions, using a random masking rate of 20%-30%. Next, the Inverse Discrete Cosine Transform (IDCT) is applied along the image dimensions to revert the data back to the spatial domain, obtaining $I^{low}(x, y)$ and $I^{high}(x, y)$. Notably, the DCT and IDCT operations are differentiable, enabling efficient computation and seamless integration into network training on both CPUs and GPUs. Details can be found in the supplementary material.

Heat-Conduction-Based Visual Encoder. High- and low-frequency information from multi-modal data is mapped to a shared thermal space and then fed into the heat-conduction-based visual encoder for thermal simulation. In most RS downstream tasks, areas containing RS objects tend to appear as high-temperature zones, while sparse or empty regions display as low-temperature zones.

The Heat Conduction Operator (HCO) simulates the process of visual information transmission as thermal conduction. The two-dimensional temperature distribution at time t , $u(x, y, t)$ is extended to a multi-dimensional feature distribution $U(x, y, c, t)$. The HCO block specifically models the general solution of physical heat conduction:

$$U_m^t = \mathcal{F}^{-1} \left(\mathcal{F}(U_m^0) e^{-k(\omega_x^2 + \omega_y^2)t} \right) \quad (1)$$

where U^0 and U^t represents the input $U(x, y, c, 0)$ and output $U(x, y, c, t)$. We denote the Discrete Fourier Transform (DFT) and its inverse (IDFT) as \mathcal{F} and \mathcal{F}^{-1} . $m \in \{o, s\}$ refers to the modality (optical or SAR). Based on the Neumann boundary condition Cheng and Cheng [2005], we replace the 2D DFT and IDFT with the 2D DCT (DCT_{2D}) and IDCT ($IDCT_{2D}$) Strang [1999]:

$$U_m^t = IDCT_{2D} \left(DCT_{2D}(U_m^0) e^{-k(\omega_x^2 + \omega_y^2)t} \right) \quad (2)$$

where $e^{-k(\omega_x^2 + \omega_y^2)t}$ functions as an adaptive filter in the frequency domain, executing heat conduction.

A set of learnable frequency value embeddings (FVEs) is predicted to estimate the heat diffusion coefficient k ($k := k(\omega_x, \omega_y)$), facilitating adaptive heat transfer, as shown in fig. 3. The weights are denoted as $W_{FVEs} \in \mathbb{R}^{M \times N \times C}$:

$$U_m^p = HCO(U_m^p, W_{FVEs}) \quad (3)$$

where U and U^p represent the temperature states of the features from different modalities before and after passing through the HCO block, respectively, with $p \in \{high, low\}$ indicating the frequency level.

To enhance the spatial representation of different structural components, we introduce a lightweight correction learner. By predicting a set of spatial correction embeddings (SCEs) from large-scale pre-trained images, it interacts with the existing temperature field and perform activation, as shown in fig. 3. The weight $W_{SCEs} \in \mathbb{R}^{M \times N \times C}$ adaptively adjusts the object boundaries in the spatial domain based on content by adding them to the original image $I(x, y)$. Given the upper-layer temperature feature Z_m^p , the correction learner can be expressed as CL :

$$Z_m^p = CL(Z_m^p, W_{SCEs}) \quad (4)$$

Where Z_m^p represents the temperature features after adaptive adjustment.

Multi-Domain Reconstruction Decoders. Considering that the restoration of heat distribution is modality-specific, the optical and SAR decoders (fig. 2 (2)), D_o^δ and D_s^δ concurrently operate on the encoded outputs ($F_o^{lp}, F_s^{lp} \in \mathbb{R}^{M \times N \times C}$). By employing convolution and pixel shuffling, decoders effectively upsample feature maps. The reconstruction outputs I' for both modalities— $I_o'^{high}, I_o'^{low}$ for optical, and $I_s'^{high}, I_s'^{low}$ for SAR—are as follows:

$$I_o'^p = D_o^\delta(F_o'^p), I_s'^p = D_s^\delta(F_s'^p) \quad (5)$$

The reconstruction is guided by the \mathcal{L}_1 loss in the frequency domain. After applying DCT, the loss \mathcal{L}_{Fre} is computed by measuring the difference between transformed features $\tilde{I}_m'^p(u, v)$ and $\tilde{I}_m^p(u, v)$.

To learn more robust higher-level features, spatial decoders (fig. 2 (3)) are responsible for fusion and reconstruction. Specifically, outputs, $F_m'^p$ and F_m^p , from the third and fourth stages extract modality-specific frequency features. The fusion layer integrates the frequency components into higher-level image features, F_m' and F_m :

$$F_m' = \text{Concat}[\text{CONV}(F_m'^{high}), \text{CONV}(F_m'^{low})], F_m = \text{Concat}[\text{CONV}(F_m^{high}), \text{CONV}(F_m^{low})] \quad (6)$$

Furthermore, the integration of multi-stage features is achieved through the function $P_m = g(F_m, F_m')$, where g combines convolution, ReLU activation and element-wise summation operations to collectively produce the final high-level output $P_m = \{P_o, P_s\}$. Subsequently, these features are fed into modality-specific spatial domain decoders D_o^ϕ and D_s^ϕ , they are upsampled to the original image size to restore the high-level semantics of the original image:

$$I_o' = D_o^\phi(P_o), I_s' = D_s^\phi(P_s) \quad (7)$$

Where I_o' and I_s' represent the reconstructed high-level optical and SAR data. The reconstruction loss in the spatial domain \mathcal{L}_{Spa} is then computed using the \mathcal{L}_1 loss.

To explore the network’s understanding of fine-grained semantic information, we employ contrastive loss to compute the semantic discrepancy between different modalities. The loss operates on embeddings F_m^p obtained from two different preprocessing methods applied to the same image, representing low- and high-frequency features. The contrastive loss \mathcal{L}_{Con} is calculated leveraging cosine similarity, following the computational methodology outlined in Atito et al. [2021].

The overall loss function is shown in eq. (8). The combined approach encourages the model to fully capture both global structures and fine-grained details:

$$\mathcal{L}_{total} = \mathcal{L}_{Con} + \mathcal{L}_{Spa} + \mathcal{L}_{Fre} \quad (8)$$

4 Experiments

4.1 Training Implementation

The training of RS-vHeat consists of self-supervised pre-training and downstream fine-tuning. The visual encoder follows the Swin-B Liu et al. [2021] configuration with four stages of 2, 2, 18, and 2 blocks. During pre-training, we use a large-scale multi-modal dataset with 450k matched optical and SAR image pairs, totaling over 3 million entries, following the methodology of RingMo Sun et al. [2022b]. The model is trained on eight A100 (80G) GPUs for 200 epochs with images of size 224. The training starts with a learning rate of 1e-6 for 10 warm-up epochs, gradually increasing to 2e-4, with a cosine annealing schedule and a minimum learning rate of 1e-5. For fine-tuning, we transfer the pre-trained embedding layers and visual encoder structure, adjusting the fixed-size FVEs and SCEs to match the image dimensions.

4.2 Performance

We comprehensively evaluate the performance of RS-vHeat compared to other representative RSFMs. Primarily, as shown in fig. 4, we analyze throughput, memory usage, and FLOPs across various image sizes. RS-vHeat (depicted by the red line) demonstrates significantly higher throughput, lower memory consumption and FLOPs, with these advantages becoming more pronounced as image sizes increase. For instance, when processing 1024×1024 resolution images, RS-vHeat achieves 2.7 times the throughput of Swin-B-based models such as SatLas Bastani et al. [2023], GFM Mendieta et al. [2023], RingMo Sun et al. [2022b], and CMID Muhtar et al. [2023], while reducing memory usage by 84%. Similarly, when compared to the improved ViT-B-based SpectralGPT Hong et al. [2024], RS-vHeat achieves 2.5 times the throughput while reducing memory usage by 77%.

Next, we evaluate the accuracy and computational efficiency of fine-tuning RS-vHeat on four tasks—semantic segmentation, object detection, classification and change detection—to demonstrate the effectiveness, along with extensive

ablation studies. Many RSFMs primarily focus on optical data and do not support SAR input, so we compare RS-vHeat with other RSFMs using optical datasets, while SAR-specific tasks are compared against specialized models. RSFMs are categorized into three main groups based on the backbone: CNN-based, ViT-based, and Swin-based. All datasets follow official partitioning methods for training and testing. More details on datasets and visualizations are provided in the supplementary materials.

Single- and Multi-Modal Semantic Segmentation. We evaluate our model on two optical datasets (Potsdam Sherrah [2016], iSAID Waqas Zamir et al. [2019]), one SAR dataset (Air-PolSAR-Seg Wang et al. [2022b]), and one multi-modal dataset (Li et al. [2022]), using UPerNet Xiao et al. [2018] with cross-entropy loss for the output head. table 1 compares RS-vHeat with 14 other RSFMs on iSAID and Potsdam. RS-vHeat demonstrates superior accuracy compared to CNN-based models, and achieves lower FLOPs than ViT-based models, exemplified by its 1.28% and 2.95% improvement over Scale-MAE Reed et al. [2023]. It also exhibits the lowest FLOPs among Swin-based models, with over a fourfold reduction in parameter count compared to SkySense Guo et al. [2024], with only 1.17% and 2.19% decreases in accuracy. Besides, on AIR-PolSAR-Seg (table 3) and WHU-OPT-SAR (table 2), RS-vHeat outperforms other specialized segmentation models, demonstrating the applicability of the heat conduction model in SAR and multi-modal segmentation tasks.

Table 1: Comparison of mF1, mIoU, parameters, and FLOPs on iSAID and Potsdam with other RSFMs.

Backbone Type	Method	Backbone	Potsdam mF1 \uparrow	iSAID mIoU \uparrow	Image Size	Params	FLOPs \downarrow
CNN-Based	GASSL (ICCV'2021) Ayush et al. [2021]	ResNet-50	91.27	65.95	896 ²	64M	722G
	SeCo (ICCV'2021) Manas et al. [2021]	ResNet-50	89.03	57.20	896 ²	64M	722G
	SSL4EO (GRSM'2023) Wang et al. [2023]	ResNet-50	91.54	64.01	896 ²	64M	722G
	CACo (CVPR'2023) Mall et al. [2023]	ResNet-18	91.35	64.32	896 ²	41M	671G
	TOV (JSTARS'2023) Tao et al. [2023]	ResNet-50	92.03	66.24	896 ²	64M	722G
	SAMRS (NeurIPS'2023) Wang et al. [2024b]	ResNet-50	91.43	66.26	896 ²	64M	722G
	RS-vHeat (Ours)	vHeat-B + SCEs	92.82	68.72	896 ²	148M	921G
ViT-Based	RVSA (TGRS'2022) Wang et al. [2022a]	ViT-B + RVSA	-	64.49	896 ²	128M	1043G
	SatMAE (NeurIPS'2022) Cong et al. [2022]	ViT-L	90.63	62.97	896 ²	341M	1536G
	Scale-MAE (ICCV'2023) Reed et al. [2023]	ViT-L	91.54	65.77	896 ²	341M	1536G
	RS-vHeat (Ours)	vHeat-B + SCEs	92.82	68.72	896 ²	148M	921G
Swin-Based	RingMo (TGRS'2022) Sun et al. [2022b]	Swin-B	91.27	67.20	896 ²	121M	968G
	SatLas (ICCV'2023) Bastani et al. [2023]	Swin-B	91.28	68.71	896 ²	121M	968G
	GFM (ICCV'2023) Mendieta et al. [2023]	Swin-B	91.85	66.62	896 ²	121M	968G
	CMID (TGRS'2023) Muhtar et al. [2023]	Swin-B	91.86	66.21	896 ²	121M	968G
	SkySense (CVPR'2024) Guo et al. [2024]	Swin-H	93.99	70.91	896 ²	>702M	>2708G
	RS-vHeat (Ours)	vHeat-B + SCEs	92.82	68.72	896 ²	148M	921G

Table 2: Comparison of OA and user’s accuracy on WHU-OPT-SAR with other specialized models.

Method	Publication	User’s Accuracy \uparrow							OA \uparrow
		Farmland	City	Village	Water	Forest	Road	Others	
SegFormer Xie et al. [2021b]	NeurIPS'2021	79.1	72.9	38.0	64.7	88.1	0.3	0.4	75.5
Segmenter Strudel et al. [2021]	ICCV'2021	82.3	75.2	51.7	74.4	89.4	16.0	12.0	79.9
MCANet Li et al. [2022]	JAG'2022	74.3	62.2	53.1	65.7	95.5	31.0	9.8	82.9
VMamba Liu et al. [2024a]	NeurIPS'2024	82.1	74.1	57.8	81.4	89.1	41.5	18.4	81.4
MMOKD Liu et al. [2024b]	TGRS'2024	70.0	58.1	50.0	69.7	80.1	40.1	25.0	82.5
RS-vHeat (Ours)	-	81.1	67.3	67.5	79.0	90.2	54.9	55.3	83.9

Table 3: Comparison of mIoU, OA, and AA on AIR-PolSAR-Seg with other specialized models.

Method	Publication	mIoU \uparrow	OA \uparrow	AA \uparrow
DeepLab V3+ Chen et al. [2018]	ECCV'2018	48.21	76.81	63.55
EncNet Zhang et al. [2018]	CVPR'2018	47.75	75.67	57.51
PSANet Zhao et al. [2018]	ECCV'2018	47.14	76.21	62.92
CCNet Huang et al. [2019]	ICCV'2019	46.46	75.53	55.83
DANet Fu et al. [2019]	CVPR'2019	51.93	76.91	62.79
GCNet Cao et al. [2019]	ICCV'2019	47.56	76.75	57.10
RS-vHeat (Ours)	-	57.46	81.46	65.92

Object Detection. We conduct coarse- and fine-grained experiments on two optical datasets (FAIR1M Sun et al. [2022a], DIOR Li et al. [2020a]) and one SAR dataset (SAR-AIRcraft-1.0 Zhirui et al. [2023]), using YOLOX Ge et al. [2021] as the output head. On the DIOR dataset, table 4 shows that RS-vHeat demonstrates not only lower FLOPs but also surpasses the results of SkySense Guo et al. [2024] by 3.57%. As shown in table 6 and table 7, RS-vHeat also achieves strong performance and high computational efficiency on two additional fine-grained datasets.

Change Detection. We train and test on the LEVIR-CD dataset Chen and Shi [2020], employing the BIT architecture Chen et al. [2021] with cross-entropy loss. RS-vHeat demonstrates superior adaptability, achieving an F1 score of

Table 4: Comparison of mAP₅₀, parameters, and FLOPs on DIOR with other RSFMs.

Backbone Type	Method	Backbone	Image Size	mAP ₅₀ ↑	Params	FLOPs ↓
CNN-Based	GASSL (ICCV'2021) Ayush et al. [2021]	ResNet-50	800 ²	67.40	41M	134G
	CACo (CVPR'2023) Mall et al. [2023]	ResNet-18	800 ²	66.91	28M	101G
	TOV (JSTARS'2023) Tao et al. [2023]	ResNet-50	800 ²	70.16	41M	134G
	SSL4EO (GRSM'2023) Wang et al. [2023]	ResNet-50	800 ²	64.82	41M	134G
	RS-vHeat (Ours)	vHeat-B + SCEs	800 ²	82.30	128M	266G
ViT-Based	RVSA (TGRS'2022) Wang et al. [2022a]	ViT-B + RVSA	800 ²	73.22	113M	378G
	SatMAE (NeurIPS'2022) Cong et al. [2022]	ViT-L	800 ²	70.89	324M	1094G
	Scale-MAE (ICCV'2023) Reed et al. [2023]	ViT-L	800 ²	73.81	324M	1094G
	RS-vHeat (Ours)	vHeat-B + SCEs	800 ²	82.30	128M	266G
Swin-Based	RingMo (TGRS'2022) Sun et al. [2022b]	Swin-B	800 ²	75.90	105M	322G
	SatLas (ICCV'2023) Bastani et al. [2023]	Swin-B	800 ²	74.10	105M	322G
	GFM (ICCV'2023) Mendieta et al. [2023]	Swin-B	800 ²	72.84	105M	322G
	CMID (TGRS'2023) Muhtar et al. [2023]	Swin-B	800 ²	75.11	105M	322G
	SkySense (CVPR'2024) Guo et al. [2024]	Swin-H	800 ²	78.73	>674M	>1679G
	RS-vHeat (Ours)	vHeat-B + SCEs	800 ²	82.30	128M	266G

Table 5: Comparison of OA, parameters, and FLOPs on AID and NWPU-RESISC45 with other RSFMs.

Backbone Type	Method	Backbone	AID		NWPU-RESISC45		Image Size	Params	FLOPs ↓
			TR=20%	TR=50%	TR=10%	TR=20%			
CNN-Based	GASSL (ICCV'2021) Ayush et al. [2021]	ResNet-50	93.55	95.92	90.86	93.06	1024 ²	24M	87G
	SeCo (ICCV'2021) Manas et al. [2021]	ResNet-50	93.47	95.99	89.64	92.91	1024 ²	24M	87G
	CACo (CVPR'2023) Mall et al. [2023]	ResNet-18	90.88	95.05	88.28	91.94	1024 ²	11M	38G
	TOV (JSTARS'2023) Tao et al. [2023]	ResNet-50	95.16	97.09	90.97	93.79	1024 ²	24M	87G
	SSL4EO (GRSM'2023) Wang et al. [2023]	ResNet-50	91.06	94.74	87.60	91.27	1024 ²	24M	87G
	RS-vHeat (Ours)	vHeat-B + SCEs	96.81	97.58	92.01	95.66	1024 ²	150M	340G
ViT-Based	RVSA (TGRS'2022) Wang et al. [2022a]	ViT-B + RVSA	97.03	98.50	93.93	95.69	1024 ²	89M	460G
	SatMAE (NeurIPS'2022) Cong et al. [2022]	ViT-L	95.02	96.94	91.72	94.10	1024 ²	310M	2070G
	Scale-MAE (ICCV'2023) Reed et al. [2023]	ViT-L	96.44	97.58	92.63	95.04	1024 ²	310M	2070G
	RS-vHeat (Ours)	vHeat-B + SCEs	96.81	97.58	92.01	95.66	1024 ²	150M	340G
Swin-Based	RingMo (TGRS'2022) Sun et al. [2022b]	Swin-B	96.90	98.34	94.25	95.67	1024 ²	87M	450G
	SatLas (ICCV'2023) Bastani et al. [2023]	Swin-B	94.96	97.38	92.16	94.70	1024 ²	87M	450G
	GFM (ICCV'2023) Mendieta et al. [2023]	Swin-B	95.47	97.09	92.73	94.64	1024 ²	87M	450G
	CMID (TGRS'2023) Muhtar et al. [2023]	Swin-B	96.11	97.79	94.05	95.53	1024 ²	87M	450G
	SkySense (CVPR'2024) Guo et al. [2024]	Swin-H	97.68	98.60	94.85	96.32	1024 ²	>660M	>2760G
	RS-vHeat (Ours)	vHeat-B + SCEs	96.81	97.58	92.01	95.66	1024 ²	150M	340G

93.48%, outperforming existing methods and surpassing SkySense Guo et al. [2024] by 0.9 points, as shown in table 8. Despite a 256-pixel input size, RS-vHeat maintains FLOPs comparable to the Swin-B-based baseline while delivering higher precision.

Image Classification. We validate our model on two benchmark datasets (AID Xia et al. [2017], NWPU-RESISC45 Cheng et al. [2017]) by attaching a classification head designed, and employ cross-entropy loss for computation. As shown in table 5, RS-vHeat surpasses CNN-based models like CACo Mall et al. [2023] in classification accuracy. Compared to ViT- and Swin-based models, RS-vHeat demonstrates superior computational efficiency while also achieving competitive accuracy.

4.3 Ablations

To validate the effectiveness of the features learned through pre-training based on heat conduction theory, we conduct ablation studies on key components.

Effectiveness of Masked Training. We visualize the accuracy curves of the visual encoder before and after introducing new structures across downstream tasks, as shown in fig. 5. All three networks are pre-trained on the same multi-modal RS data. In (a), we use vHeat-B with the SimMIM Xie et al. [2022] pixel mask training scheme; in (b), we add frequency domain masking and multi-domain reconstruction; and in (c), we integrate the innovative RS-vHeat structure, which includes SCEs. For optical tasks, RS-vHeat shows faster accuracy improvement, stabilizing at a higher ceiling. It

Table 6: Comparison of mAP₅₀ and mAP₇₅ on SAR-AIRcraft-1.0 with other specialized models.

Method	Publication	mAP ₅₀ ↑	mAP ₇₅ ↑
Faster R-CNN	Ren et al. [2016]	76.1	62.2
Cascade R-CNN	Cai and Vasconcelos [2018]	75.7	58.9
RepPoints	Yang et al. [2019]	72.6	53.3
SKG-Net	Fu et al. [2021]	70.7	46.4
SA-Net	Zhirui et al. [2023]	77.7	62.8
RS-vHeat (Ours)	-	87.1	67.4

Table 7: Comparison of mAP, parameters, and FLOPs on FAIR1M-2.0 with other RSFMs.

Method	Backbone	mAP \uparrow	Params	FLOPs \downarrow
CACo Mall et al. [2023]	ResNet-18	47.83	42M	64G
GASSL Ayush et al. [2021]	ResNet-50	48.15	55M	77G
TOV Tao et al. [2023]	ResNet-50	49.62	55M	77G
SSL4EO Wang et al. [2023]	ResNet-50	49.37	55M	77G
RVSA Wang et al. [2022a]	ViT-B + RVSA	47.04	126M	160G
SatMAE Cong et al. [2022]	ViT-L	46.55	336M	241G
Scale-MAE Reed et al. [2023]	ViT-L	48.31	336M	241G
SatLas Bastani et al. [2023]	Swin-B	46.19	119M	167G
GFM Mendieta et al. [2023]	Swin-B	49.69	119M	167G
RingMo Sun et al. [2022b]	Swin-B	46.21	119M	167G
CMID Muhtar et al. [2023]	Swin-B	50.58	119M	167G
SkySense Guo et al. [2024]	Swin-H	54.57	>688M	>900G
RS-vHeat	vHeat-B + SCEs	48.29	130M	137G

Table 8: Comparison of F1 on LEVIR-CD with other RSFMs.

Method	Backbone	F1 \uparrow	Params	FLOPs \downarrow
CACo Mall et al. [2023]	ResNet-18	81.04	12M	11G
GASSL Ayush et al. [2021]	ResNet-50	78.19	27M	25G
SeCo Manas et al. [2021]	ResNet-50	90.14	27M	25G
SSL4EO Wang et al. [2023]	ResNet-50	89.05	27M	25G
RVSA Wang et al. [2022a]	ViT-B + RVSA	90.86	94M	57G
SatMAE Cong et al. [2022]	ViT-L	87.65	304M	162G
Scale-MAE Reed et al. [2023]	ViT-L	92.07	304M	162G
SatLas Bastani et al. [2023]	Swin-B	90.62	88M	45G
GFM Mendieta et al. [2023]	Swin-B	91.73	88M	45G
RingMo Sun et al. [2022b]	Swin-B	91.86	88M	45G
CMID Muhtar et al. [2023]	Swin-B	91.72	88M	45G
SkySense Guo et al. [2024]	Swin-H	92.58	>656M	>307G
RS-vHeat (Ours)	vHeat-B + SCEs	93.48	93M	46G

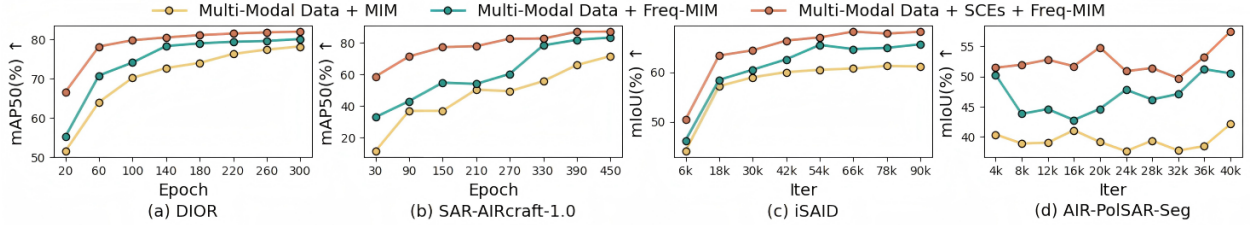


Figure 5: Accuracy curves of various methods across modalities. (a) optical object detection on DIOR, (b) SAR object detection on SAR-AIRcraft-1.0, (c) optical semantic segmentation on iSAID, and (d) SAR semantic segmentation on AIR-PolSAR-Seg.

surpasses 80% mAP₅₀ on the DIOR dataset by the 120th epoch. For SAR tasks, while there are fluctuations, RS-vHeat demonstrates better adaptability and prediction accuracy. Overall, the improvements in pre-training and SCEs lead to advanced feature extraction performance.

Reconstruction Learning Strategy. table 9 demonstrates the effectiveness of different loss components—spatial domain reconstruction loss (SDR), frequency domain reconstruction loss (FDR), and contrastive loss (CL). When only SDR is applied (row a), performance drops slightly on both optical and SAR datasets. Adding FDR (row b) improves performance by leveraging frequency domain information. Introducing CL (row c) further enhances performance by enforcing similarity constraints in the multi-modal feature space, improving feature learning. This leads to an 83.9% OA on WHU-OPT-SAR, surpassing rows (a) and (b) by 3.4% and 1.6%, respectively. These results highlight the importance of combining these three losses for improved predictions across tasks and modalities.

Table 9: Results of RS-vHeat under various constraints of self-supervised learning strategies.

#	Loss			Object Detection			Semantic Segmentation		
				DIOR (Optical)	SAR-AIRcraft-1.0 (SAR)	iSAID (Optical)	AIR-PolSAR-Seg (SAR)	WHU-OPT-SAR (Optical+SAR)	
	SDR	FDR	CL	mAP ₅₀ \uparrow	mAP ₅₀ \uparrow	mIoU \uparrow	mIoU \uparrow	OA \uparrow	
(a)	✓	✗	✗	78.2	84.6	66.1	54.7	80.5	
(b)	✓	✓	✗	79.5	86.4	67.2	55.1	82.3	
(c)	✓	✓	✓	82.3	87.1	68.7	57.5	83.9	

5 Conclusion

In this work, we introduce the concept of heat conduction into RS tasks for the first time and establish a multi-modal RSFM, RS-vHeat. By employing a self-supervised learning strategy that integrates frequency domain masking and multi-domain reconstruction, along with a heat conduction operator incorporating spatial correction embeddings, we propose an approach that balances computational complexity and global receptive field coverage in RS. Our method captures global details from both spatial and frequency domains, significantly reducing the issue of small object omission, and achieves consistent multi-modal feature representation by mapping images into a high-dimensional thermal space. In future work, we plan to propose new solutions that offer fresh insights and methods for tackling visual modeling challenges across various industries.

References

- Jamie Sherrah. Fully convolutional networks for dense semantic labelling of high-resolution aerial imagery. *arXiv preprint arXiv:1606.02585*, 2016.
- Yuxiang Zhang, Wei Li, Ran Tao, Jiangtao Peng, Qian Du, and Zhaoquan Cai. Cross-scene hyperspectral image classification with discriminative cooperative alignment. *IEEE Transactions on Geoscience and Remote Sensing*, 59(11):9646–9660, 2021.
- Xian Sun, Peijin Wang, Zhiyuan Yan, Feng Xu, Ruiping Wang, Wenhui Diao, Jin Chen, Jihao Li, Yingchao Feng, Tao Xu, et al. Fair1m: A benchmark dataset for fine-grained object recognition in high-resolution remote sensing imagery. *ISPRS Journal of Photogrammetry and Remote Sensing*, 184:116–130, 2022a.
- Ke Li, Gang Wan, Gong Cheng, Liqiu Meng, and Junwei Han. Object detection in optical remote sensing images: A survey and a new benchmark. *ISPRS journal of photogrammetry and remote sensing*, 159:296–307, 2020a.
- Xiaonan Lu, Xian Sun, Wenhui Diao, Yingchao Feng, Peijin Wang, and Kun Fu. Lil: Lightweight incremental learning approach through feature transfer for remote sensing image scene classification. *IEEE Transactions on Geoscience and Remote Sensing*, 60:1–20, 2021.
- Xian Sun, Peijin Wang, Cheng Wang, Yingfei Liu, and Kun Fu. Pbnnet: Part-based convolutional neural network for complex composite object detection in remote sensing imagery. *ISPRS Journal of Photogrammetry and Remote Sensing*, 173:50–65, 2021.
- Kun FU, Xian SUN, Xiaolan QIU, Wenhui DIAO, Zhiyuan YAN, Lijia HUANG, and Hongfeng YU. Multi-satellite integrated processing and analysis method under remote sensing big data. *National Remote Sensing Bulletin*, 25(3): 691–707, 2021. doi:10.11834/jrs.20211058.
- Wenyuan Li, Keyan Chen, Hao Chen, and Zhenwei Shi. Geographical knowledge-driven representation learning for remote sensing images. *IEEE Transactions on Geoscience and Remote Sensing*, 60:1–16, 2021.
- Oscar Manas, Alexandre Lacoste, Xavier Giró-i Nieto, David Vazquez, and Pau Rodriguez. Seasonal contrast: Unsupervised pre-training from uncurated remote sensing data. In *Proceedings of the IEEE/CVF International Conference on Computer Vision*, pages 9414–9423, 2021.
- Utkarsh Mall, Bharath Hariharan, and Kavita Bala. Change-aware sampling and contrastive learning for satellite images. In *Proceedings of the IEEE/CVF Conference on Computer Vision and Pattern Recognition*, pages 5261–5270, 2023.
- Kumar Ayush, Burak Uzkent, Chenlin Meng, Kumar Tanmay, Marshall Burke, David Lobell, and Stefano Ermon. Geography-aware self-supervised learning. In *Proceedings of the IEEE/CVF International Conference on Computer Vision*, pages 10181–10190, 2021.
- Yezhen Cong, Samar Khanna, Chenlin Meng, Patrick Liu, Erik Rozi, Yutong He, Marshall Burke, David Lobell, and Stefano Ermon. Satmae: Pre-training transformers for temporal and multi-spectral satellite imagery. *Advances in Neural Information Processing Systems*, 35:197–211, 2022.
- Di Wang, Qiming Zhang, Yufei Xu, Jing Zhang, Bo Du, Dacheng Tao, and Liangpei Zhang. Advancing plain vision transformer toward remote sensing foundation model. *IEEE Transactions on Geoscience and Remote Sensing*, 61: 1–15, 2022a.
- Chao Tao, Ji Qi, Guo Zhang, Qing Zhu, Weipeng Lu, and Haifeng Li. Tov: The original vision model for optical remote sensing image understanding via self-supervised learning. *IEEE Journal of Selected Topics in Applied Earth Observations and Remote Sensing*, 16:4916–4930, 2023.
- Colorado J Reed, Ritwik Gupta, Shufan Li, Sarah Brockman, Christopher Funk, Brian Clipp, Kurt Keutzer, Salvatore Candido, Matt Uyttendaele, and Trevor Darrell. Scale-mae: A scale-aware masked autoencoder for multiscale geospatial representation learning. In *Proceedings of the IEEE/CVF International Conference on Computer Vision*, pages 4088–4099, 2023.

- Matías Mendieta, Boran Han, Xingjian Shi, Yi Zhu, and Chen Chen. Towards geospatial foundation models via continual pretraining. In *Proceedings of the IEEE/CVF International Conference on Computer Vision*, pages 16806–16816, 2023.
- Favyen Bastani, Piper Wolters, Ritwik Gupta, Joe Ferdinando, and Aniruddha Kembhavi. Satlaspretrain: A large-scale dataset for remote sensing image understanding. In *Proceedings of the IEEE/CVF International Conference on Computer Vision*, pages 16772–16782, 2023.
- Kaiming He, Xiangyu Zhang, Shaoqing Ren, and Jian Sun. Deep residual learning for image recognition. In *Proceedings of the IEEE conference on computer vision and pattern recognition*, pages 770–778, 2016.
- Alexey Dosovitskiy, Lucas Beyer, Alexander Kolesnikov, Dirk Weissenborn, Xiaohua Zhai, Thomas Unterthiner, Mostafa Dehghani, Matthias Minderer, Georg Heigold, Sylvain Gelly, et al. An image is worth 16x16 words: Transformers for image recognition at scale. *arXiv preprint arXiv:2010.11929*, 2020.
- Ze Liu, Yutong Lin, Yue Cao, Han Hu, Yixuan Wei, Zheng Zhang, Stephen Lin, and Baining Guo. Swin transformer: Hierarchical vision transformer using shifted windows. In *Proceedings of the IEEE/CVF international conference on computer vision*, pages 10012–10022, 2021.
- Ashish Vaswani, Noam Shazeer, Niki Parmar, Jakob Uszkoreit, Llion Jones, Aidan N Gomez, Łukasz Kaiser, and Illia Polosukhin. Attention is all you need. *Advances in neural information processing systems*, 30, 2017.
- Wenjie Luo, Yujia Li, Raquel Urtasun, and Richard Zemel. Understanding the effective receptive field in deep convolutional neural networks. In D. Lee, M. Sugiyama, U. Luxburg, I. Guyon, and R. Garnett, editors, *Advances in Neural Information Processing Systems*, volume 29. Curran Associates, Inc., 2016. URL https://proceedings.neurips.cc/paper_files/paper/2016/file/c8067ad1937f728f51288b3eb986afaa-Paper.pdf.
- Emmanuel Christophe, Julien Michel, and Jordi Inglada. Remote sensing processing: From multicore to gpu. *IEEE Journal of Selected Topics in Applied Earth Observations and Remote Sensing*, 4(3):643–652, 2011.
- Yan Ma, Haiping Wu, Lizhe Wang, Bormin Huang, Rajiv Ranjan, Albert Zomaya, and Wei Jie. Remote sensing big data computing: Challenges and opportunities. *Future Generation Computer Systems*, 51:47–60, 2015. ISSN 0167-739X. doi:<https://doi.org/10.1016/j.future.2014.10.029>. URL <https://www.sciencedirect.com/science/article/pii/S0167739X14002234>. Special Section: A Note on New Trends in Data-Aware Scheduling and Resource Provisioning in Modern HPC Systems.
- Jiang Li and Ram M Narayanan. A shape-based approach to change detection of lakes using time series remote sensing images. *IEEE transactions on geoscience and remote sensing*, 41(11):2466–2477, 2003.
- Huanfeng Shen, Menghui Jiang, Jie Li, Chenxia Zhou, Qiangqiang Yuan, and Liangpei Zhang. Coupling model- and data-driven methods for remote sensing image restoration and fusion: Improving physical interpretability. *IEEE Geoscience and Remote Sensing Magazine*, 10(2):231–249, 2022. doi:10.1109/MGRS.2021.3135954.
- Anastasios Temenos, Nikos Temenos, Maria Kaselimi, Anastasios Doulamis, and Nikolaos Doulamis. Interpretable deep learning framework for land use and land cover classification in remote sensing using shap. *IEEE Geoscience and Remote Sensing Letters*, 20:1–5, 2023. doi:10.1109/LGRS.2023.3251652.
- Adrián Pérez-Suay, Jose E. Adsuara, María Piles, Laura Martínez-Ferrer, Emiliano Díaz, Alvaro Moreno-Martínez, and Gustau Camps-Valls. Interpretability of recurrent neural networks in remote sensing. In *IGARSS 2020 - 2020 IEEE International Geoscience and Remote Sensing Symposium*, pages 3991–3994, 2020. doi:10.1109/IGARSS39084.2020.9323898.
- Zhaozhi Wang, Yue Liu, Yunfan Liu, Hongtian Yu, Yaowei Wang, Qixiang Ye, and Yunjie Tian. wheat: Building vision models upon heat conduction. *arXiv preprint arXiv:2405.16555*, 2024a.
- Chi Zhang, Shiqing Wei, Shunping Ji, and Meng Lu. Detecting large-scale urban land cover changes from very high resolution remote sensing images using cnn-based classification. *ISPRS International Journal of Geo-Information*, 8(4):189, 2019.
- Haifeng Li, Haikuo Huang, Li Chen, Jian Peng, Haozhe Huang, Zhenqi Cui, Xiaoming Mei, and Guohua Wu. Adversarial examples for cnn-based sar image classification: An experience study. *IEEE Journal of Selected Topics in Applied Earth Observations and Remote Sensing*, 14:1333–1347, 2020b.
- Xiaohu Dong, Ruigang Fu, Yinghui Gao, Yao Qin, Yuanxin Ye, and Biao Li. Remote sensing object detection based on receptive field expansion block. *IEEE Geoscience and Remote Sensing Letters*, 19:1–5, 2021.
- Xi Chen, Zhiqiang Li, Jie Jiang, Zhen Han, Shiyi Deng, Zhihong Li, Tao Fang, Hong Huo, Qingli Li, and Min Liu. Adaptive effective receptive field convolution for semantic segmentation of vhr remote sensing images. *IEEE Transactions on Geoscience and Remote Sensing*, 59(4):3532–3546, 2020.

- Tianyu Yan, Zifu Wan, and Pingping Zhang. Fully transformer network for change detection of remote sensing images. In *Proceedings of the Asian Conference on Computer Vision*, pages 1691–1708, 2022.
- Albert Gu, Karan Goel, and Christopher Ré. Efficiently modeling long sequences with structured state spaces. *arXiv preprint arXiv:2111.00396*, 2021.
- Yue Liu, Yunjie Tian, Yuzhong Zhao, Hongtian Yu, Lingxi Xie, Yaowei Wang, Qixiang Ye, and Yunfan Liu. Vmamba: Visual state space model, 2024a. URL <https://arxiv.org/abs/2401.10166>.
- Lianghui Zhu, Bencheng Liao, Qian Zhang, Xinlong Wang, Wenyu Liu, and Xinggang Wang. Vision mamba: Efficient visual representation learning with bidirectional state space model. *arXiv preprint arXiv:2401.09417*, 2024a.
- Albert Gu and Tri Dao. Mamba: Linear-time sequence modeling with selective state spaces. *arXiv preprint arXiv:2312.00752*, 2023.
- Rui Xu, Shu Yang, Yihui Wang, Bo Du, and Hao Chen. A survey on vision mamba: Models, applications and challenges. *arXiv preprint arXiv:2404.18861*, 2024.
- Keyan Chen, Bowen Chen, Chenyang Liu, Wenyuan Li, Zhengxia Zou, and Zhenwei Shi. Rsmamba: Remote sensing image classification with state space model. *IEEE Geoscience and Remote Sensing Letters*, 2024a.
- Qinfeng Zhu, Yuanzhi Cai, Yuan Fang, Yihan Yang, Cheng Chen, Lei Fan, and Anh Nguyen. Samba: Semantic segmentation of remotely sensed images with state space model. *arXiv preprint arXiv:2404.01705*, 2024b.
- Hongruixuan Chen, Jian Song, Chengxi Han, Junshi Xia, and Naoto Yokoya. Changemamba: Remote sensing change detection with spatio-temporal state space model. *arXiv preprint arXiv:2404.03425*, 2024b.
- Xin Guo, Jiangwei Lao, Bo Dang, Yingying Zhang, Lei Yu, Lixiang Ru, Liheng Zhong, Ziyuan Huang, Kang Wu, Dingxiang Hu, et al. Skysense: A multi-modal remote sensing foundation model towards universal interpretation for earth observation imagery. In *Proceedings of the IEEE/CVF Conference on Computer Vision and Pattern Recognition*, pages 27672–27683, 2024.
- Xian Sun, Peijin Wang, Wanxuan Lu, Zicong Zhu, Xiaonan Lu, Qibin He, Junxi Li, Xuee Rong, Zhujun Yang, Hao Chang, et al. Ringmo: A remote sensing foundation model with masked image modeling. *IEEE Transactions on Geoscience and Remote Sensing*, 2022b.
- Danfeng Hong, Bing Zhang, Xuyang Li, Yuxuan Li, Chenyu Li, Jing Yao, Naoto Yokoya, Hao Li, Pedram Ghamisi, Xiuping Jia, et al. Spectralgpt: Spectral remote sensing foundation model. *IEEE Transactions on Pattern Analysis and Machine Intelligence*, 2024.
- Zhenda Xie, Zheng Zhang, Yue Cao, Yutong Lin, Jianmin Bao, Zhuliang Yao, Qi Dai, and Han Hu. Simmim: A simple framework for masked image modeling. In *Proceedings of the IEEE/CVF conference on computer vision and pattern recognition*, pages 9653–9663, 2022.
- Wenbin Xie, Dehua Song, Chang Xu, Chunjing Xu, Hui Zhang, and Yunhe Wang. Learning frequency-aware dynamic network for efficient super-resolution. In *Proceedings of the IEEE/CVF International Conference on Computer Vision*, pages 4308–4317, 2021a.
- Alexander H-D Cheng and Daisy T Cheng. Heritage and early history of the boundary element method. *Engineering analysis with boundary elements*, 29(3):268–302, 2005.
- Gilbert Strang. The discrete cosine transform. *SIAM review*, 41(1):135–147, 1999.
- Sara Atito, Muhammad Awais, and Josef Kittler. Sit: Self-supervised vision transformer. *arXiv preprint arXiv:2104.03602*, 2021.
- Dilxat Muhtar, Xueliang Zhang, Pengfeng Xiao, Zhenshi Li, and Feng Gu. Cmid: A unified self-supervised learning framework for remote sensing image understanding. *IEEE Transactions on Geoscience and Remote Sensing*, 61: 1–17, 2023.
- Syed Waqas Zamir, Aditya Arora, Akshita Gupta, Salman Khan, Guolei Sun, Fahad Shahbaz Khan, Fan Zhu, Ling Shao, Gui-Song Xia, and Xiang Bai. isaid: A large-scale dataset for instance segmentation in aerial images. In *Proceedings of the IEEE/CVF Conference on Computer Vision and Pattern Recognition Workshops*, pages 28–37, 2019.
- Zhirui Wang, Xuan Zeng, Zhiyuan Yan, Jian Kang, and Xian Sun. Air-polsar-seg: A large-scale data set for terrain segmentation in complex-scene polsar images. *IEEE Journal of Selected Topics in Applied Earth Observations and Remote Sensing*, 15:3830–3841, 2022b.
- Xue Li, Guo Zhang, Hao Cui, Shasha Hou, Shunyao Wang, Xin Li, Yujia Chen, Zhijiang Li, and Li Zhang. Mcanet: A joint semantic segmentation framework of optical and sar images for land use classification. *International Journal of Applied Earth Observation and Geoinformation*, 106:102638, 2022.

- Tete Xiao, Yingcheng Liu, Bolei Zhou, Yuning Jiang, and Jian Sun. Unified perceptual parsing for scene understanding. In *Proceedings of the European Conference on Computer Vision (ECCV)*, September 2018.
- Yi Wang, Nassim Ait Ali Braham, Zhitong Xiong, Chenying Liu, Conrad M Albrecht, and Xiao Xiang Zhu. Ssl4eo-s12: A large-scale multimodal, multitemporal dataset for self-supervised learning in earth observation [software and data sets]. *IEEE Geoscience and Remote Sensing Magazine*, 11(3):98–106, 2023.
- Di Wang, Jing Zhang, Bo Du, Minqiang Xu, Lin Liu, Dacheng Tao, and Liangpei Zhang. Samrs: Scaling-up remote sensing segmentation dataset with segment anything model. *Advances in Neural Information Processing Systems*, 36, 2024b.
- Enze Xie, Wenhai Wang, Zhiding Yu, Anima Anandkumar, Jose M Alvarez, and Ping Luo. Segformer: Simple and efficient design for semantic segmentation with transformers. *Advances in neural information processing systems*, 34:12077–12090, 2021b.
- Robin Strudel, Ricardo Garcia, Ivan Laptev, and Cordelia Schmid. Segmenter: Transformer for semantic segmentation. In *Proceedings of the IEEE/CVF International Conference on Computer Vision*, pages 7262–7272, 2021.
- Xiao Liu, Fei Jin, Shuxiang Wang, Jie Rui, Xibing Zuo, Xiaobing Yang, and Chuanxiang Cheng. Multimodal online knowledge distillation framework for land use/cover classification using full or missing modalities. *IEEE Transactions on Geoscience and Remote Sensing*, 2024b.
- Liang-Chieh Chen, Yukun Zhu, George Papandreou, Florian Schroff, and Hartwig Adam. Encoder-decoder with atrous separable convolution for semantic image segmentation. In *Proceedings of the European conference on computer vision (ECCV)*, pages 801–818, 2018.
- Hang Zhang, Kristin Dana, Jianping Shi, Zhongyue Zhang, Xiaogang Wang, Amrbrish Tyagi, and Amit Agrawal. Context encoding for semantic segmentation. In *Proceedings of the IEEE conference on Computer Vision and Pattern Recognition*, pages 7151–7160, 2018.
- Hengshuang Zhao, Yi Zhang, Shu Liu, Jianping Shi, Chen Change Loy, Dahua Lin, and Jiaya Jia. Pscanet: Point-wise spatial attention network for scene parsing. In *Proceedings of the European conference on computer vision (ECCV)*, pages 267–283, 2018.
- Zilong Huang, Xinggang Wang, Lichao Huang, Chang Huang, Yunchao Wei, and Wenyu Liu. Ccnet: Criss-cross attention for semantic segmentation. In *Proceedings of the IEEE/CVF international conference on computer vision*, pages 603–612, 2019.
- Jun Fu, Jing Liu, Haijie Tian, Yong Li, Yongjun Bao, Zhiwei Fang, and Hanqing Lu. Dual attention network for scene segmentation. In *Proceedings of the IEEE/CVF conference on computer vision and pattern recognition*, pages 3146–3154, 2019.
- Yue Cao, Jiarui Xu, Stephen Lin, Fangyun Wei, and Han Hu. Gcnet: Non-local networks meet squeeze-excitation networks and beyond. In *Proceedings of the IEEE/CVF international conference on computer vision workshops*, pages 0–0, 2019.
- Wang Zhirui, Kang Yuzhuo, Zeng Xuan, WANG Yuelei, ZHANG Ting, and SUN Xian. Sar-aircraft-1.0: High-resolution sar aircraft detection and recognition dataset. *Journal of Radars*, 12(4):906–922, 2023.
- Zheng Ge, Songtao Liu, Feng Wang, Zeming Li, and Jian Sun. Yolox: Exceeding yolo series in 2021. *arXiv preprint arXiv:2107.08430*, 2021.
- Shaoqing Ren, Kaiming He, Ross Girshick, and Jian Sun. Faster r-cnn: Towards real-time object detection with region proposal networks. *IEEE transactions on pattern analysis and machine intelligence*, 39(6):1137–1149, 2016.
- Zhaowei Cai and Nuno Vasconcelos. Cascade r-cnn: Delving into high quality object detection. In *Proceedings of the IEEE conference on computer vision and pattern recognition*, pages 6154–6162, 2018.
- Ze Yang, Shaohui Liu, Han Hu, Liwei Wang, and Stephen Lin. Reppoints: Point set representation for object detection. In *Proceedings of the IEEE/CVF international conference on computer vision*, pages 9657–9666, 2019.
- Kun Fu, Jiamei Fu, Zhirui Wang, and Xian Sun. Scattering-keypoint-guided network for oriented ship detection in high-resolution and large-scale sar images. *IEEE Journal of Selected Topics in Applied Earth Observations and Remote Sensing*, 14:11162–11178, 2021.
- Hao Chen and Zhenwei Shi. A spatial-temporal attention-based method and a new dataset for remote sensing image change detection. *Remote Sensing*, 12(10), 2020. ISSN 2072-4292. doi:10.3390/rs12101662. URL <https://www.mdpi.com/2072-4292/12/10/1662>.
- Hao Chen, Zipeng Qi, and Zhenwei Shi. Remote sensing image change detection with transformers. *IEEE Transactions on Geoscience and Remote Sensing*, 60:1–14, 2021.

-
- Gui-Song Xia, Jingwen Hu, Fan Hu, Baoguang Shi, Xiang Bai, Yanfei Zhong, Liangpei Zhang, and Xiaoqiang Lu. Aid: A benchmark data set for performance evaluation of aerial scene classification. *IEEE Transactions on Geoscience and Remote Sensing*, 55(7):3965–3981, 2017.
- Gong Cheng, Junwei Han, and Xiaoqiang Lu. Remote sensing image scene classification: Benchmark and state of the art. *Proceedings of the IEEE*, 105(10):1865–1883, 2017.
- Xingxing Xie, Gong Cheng, Jiabao Wang, Xiwen Yao, and Junwei Han. Oriented r-cnn for object detection. In *Proceedings of the IEEE/CVF international conference on computer vision*, pages 3520–3529, 2021c.

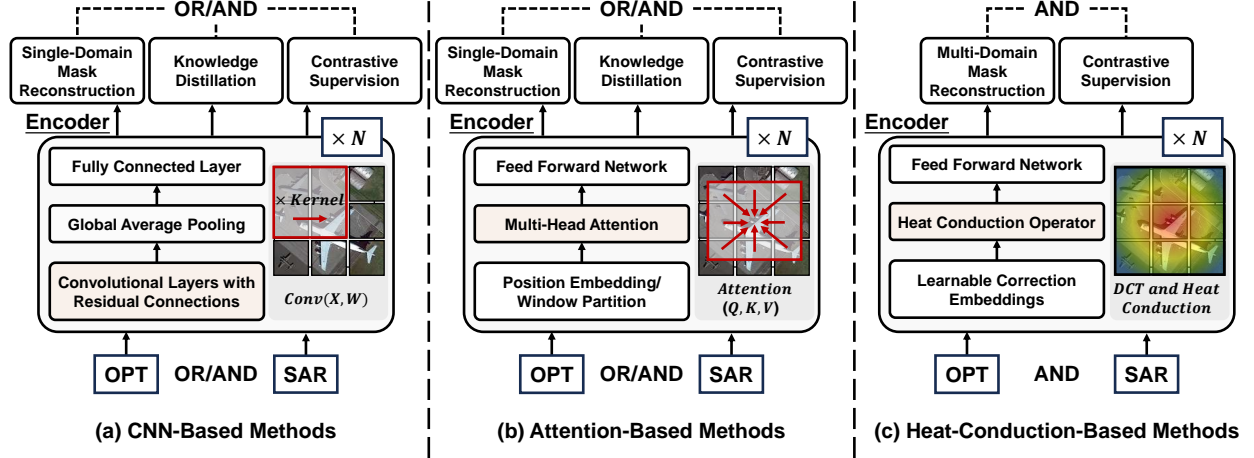


Figure 6: Comparison of the self-supervised training scheme for the heat-conduction-based RFSM with other methods. (a) CNN-Based methods Li et al. [2021], Manas et al. [2021], Mall et al. [2023], Ayush et al. [2021]. (b) Attention-Based methods Cong et al. [2022], Wang et al. [2022a], Tao et al. [2023], Reed et al. [2023], Mendieta et al. [2023], Bastani et al. [2023]. (c) Heat-Conduction-Based method (ours). In our visual encoder, the heat conduction operator is employed to replace the residual blocks in CNN-based networks, and the attention layers in attention-based networks. For optical (OPT) and SAR inputs, the dual constraints of multi-domain mask reconstruction and distance metrics for multi-modal feature representations provide self-supervised signals during the pre-training process. This approach transforms the visual semantic propagation into a process of thermal diffusion within a thermal space, guided by the scene and object characteristics, dynamically extracting global information across the entire image.

A. Comparison details among RFSMs with different backbone networks

Previous research on RFSMs primarily utilized existing visual encoders to extract deep features, integrating various self-supervised learning strategies with decoder structures, and pre-training on large-scale RS datasets. Visual encoders, as the core components of these models, are generally divided into two categories in recent research: 1) CNN-based methods Li et al. [2021], Manas et al. [2021], Mall et al. [2023], Ayush et al. [2021], as shown in fig. 6 (a). These models typically adopt the ResNet18/50 framework He et al. [2016], with the residual module serving as the key learning structure. These approaches extract rich information from RS data through pixel masking reconstruction, expert geographical knowledge supervision or contrastive learning signals. 2) Attention-based methods, such as Cong et al. [2022], Wang et al. [2022a], Tao et al. [2023], Reed et al. [2023], Mendieta et al. [2023] and Bastani et al. [2023], as illustrated in fig. 6 (b). These models primarily utilize the ViT Dosovitskiy et al. [2020] and Swin Transformers Liu et al. [2021] as visual encoders, where the fundamental modules rely on attention mechanisms Vaswani et al. [2017] and feed forward networks (FFNs) to model global dependencies. Pre-training is typically conducted through masked reconstruction, knowledge distillation or contrastive signals to enhance the robustness of the model representations.

In summary, current RFSMs typically employ CNN-based or attention-based methods as visual encoders, innovating in learning and training strategies to enhance model performance. As shown in fig. 6 (c), RS-vHeat employs a heat-conduction-based visual encoder, with the heat conduction operator serving as the core computational module. During self-supervised learning, it applies frequency-domain and spatial-domain masking reconstruction constraints, along with an additional contrastive loss, which differentiates it significantly from existing RFSMs.

B. Preliminary of heat conduction

Inspired by the physical principle of heat conduction, vHeat Wang et al. [2024a] considers a region as a two-dimensional region $D \in \mathbb{R}^2$. Then, for each point (x, y) in the region, its temperature is $u(x, y, t)$ at time t , and the initial condition is $t = 0$. The heat conduction propagation on this region can be expressed:

$$\frac{\partial u}{\partial t} = k \left(\frac{\partial^2 u}{\partial x^2} + \frac{\partial^2 u}{\partial y^2} \right) \quad (9)$$

where k represents the thermal diffusivity. We denote the Fourier Transform and its inverse using the symbols \mathcal{F} and \mathcal{F}^{-1} , respectively. After taking the Fourier Transform on both sides of the equals sign in eq. (9), we formulate the

calculation of physical heat equation as:

$$\mathcal{F}\left(\frac{\partial u}{\partial t}\right) = k\mathcal{F}\left(\frac{\partial^2 u}{\partial x^2} + \frac{\partial^2 u}{\partial y^2}\right) \quad (10)$$

We represent the result of the Fourier transform of $u(x, y, t)$ as follows:

$$\tilde{u}(\omega_x, \omega_y, t) := \mathcal{F}(u(x, y, t)) \quad (11)$$

The left and right of eq. (10) can be reformulated as

$$\mathcal{F}\left(\frac{\partial u}{\partial t}\right) = \frac{\partial \tilde{u}(\omega_x, \omega_y, t)}{\partial t} \quad (12)$$

$$\mathcal{F}\left(\frac{\partial^2 u}{\partial x^2} + \frac{\partial^2 u}{\partial y^2}\right) = -(\omega_x^2 + \omega_y^2)\tilde{u}(\omega_x, \omega_y, t) \quad (13)$$

Furthermore, the eq. (10) is expressed as an ordinary differential equation in the frequency domain:

$$\frac{d\tilde{u}(\omega_x, \omega_y, t)}{dt} = -k(\omega_x^2 + \omega_y^2)\tilde{u}(\omega_x, \omega_y, t) \quad (14)$$

To solve $\tilde{u}(\omega_x, \omega_y, t)$ in eq. (14), we use $\tilde{f}(\omega_x, \omega_y)$ to represent the Fourier Transform of $f(x, y)$, and we can get the following result under the initial condition of $\tilde{u}(\omega_x, \omega_y, t)|_{t=0}$:

$$\tilde{u}(\omega_x, \omega_y, t) = \tilde{f}(\omega_x, \omega_y)e^{-k(\omega_x^2 + \omega_y^2)t} \quad (15)$$

Finally, the values in the frequency domain are converted back to the space domain by inverse Fourier Transform, and we get the general solution of heat equation in the spatial domain expressed as follows:

$$u(x, y, t) = \mathcal{F}^{-1}(\tilde{f}(\omega_x, \omega_y)e^{-k(\omega_x^2 + \omega_y^2)t}) = \frac{1}{4\pi^2} \int_{\tilde{D}} \tilde{f}(\omega_x, \omega_y)e^{-k(\omega_x^2 + \omega_y^2)t} e^{i(\omega_x x + \omega_y y)} d\omega_x d\omega_y \quad (16)$$

C. Implementation details of the masking strategy

Given the multi-modal input (optical and SAR), denoted as $I(x, y, c) = \{I_o, I_s\}$, $I_o \in \mathbb{R}^{H \times W \times 3}$, $I_s \in \mathbb{R}^{H \times W \times 1}$, the process begins by applying the DCT along each image dimension $c = 1, \dots, C$, extracting 2D planes from the spatial domain $I(x, y)$ and converting them into its frequency representation $\tilde{I}(u, v)$. This transformation concentrates low-frequency information in the top-left corner of the frequency spectrum:

$$\tilde{I}(u, v) = \frac{2}{\sqrt{MN}} \sum_{x=0}^{M-1} \sum_{y=0}^{N-1} I(x, y) \cos \frac{(2x+1)u\pi}{2M} \cos \frac{(2y+1)v\pi}{2N} \quad (17)$$

where M and N denote the width and height of the input image, respectively.

To address signals across different frequency ranges, we apply a sector mask to the transformed image. Centered at the top-left, this mask separates the image into distinct high-frequency $\tilde{I}^{high}(u, v)$ and low-frequency $\tilde{I}^{low}(u, v)$ regions:

$$\tilde{I}^{low}(u, v), \tilde{I}^{high}(u, v) = \tilde{M} \odot \tilde{I}(u, v) \quad (18)$$

The binary mask \tilde{M} , sized $(M \times N)$, is applied to each dimension c using the operator \odot . Each element of \tilde{M} takes a value of either 0 or 1.

After applying the mask, we perform the IDCT to convert the processed frequency representation back to its spatial representation along each dimension:

$$I^{low}(x, y) = \sum_{u=0}^{M-1} \sum_{v=0}^{N-1} \frac{2}{\sqrt{MN}} \tilde{I}^{low}(u, v) \cos \frac{(2x+1)u\pi}{2M} \cos \frac{(2y+1)v\pi}{2N} \quad (19)$$

$$I^{high}(x, y) = \sum_{u=0}^{M-1} \sum_{v=0}^{N-1} \frac{2}{\sqrt{MN}} \tilde{I}^{high}(u, v) \cos \frac{(2x+1)u\pi}{2M} \cos \frac{(2y+1)v\pi}{2N} \quad (20)$$

Where $I^{low}(x, y)$ and $I^{high}(x, y)$ denote the low- and high-frequency representation that are converted back to their spatial domain after applying the mask. The results are then concatenated to restore the original dimensionality.

D. Configuration and visualization results of fownstream task datasets

RS-vHeat is trained on 10 datasets across 4 downstream tasks. In this section, we provide detailed information about the datasets and experimental configurations.

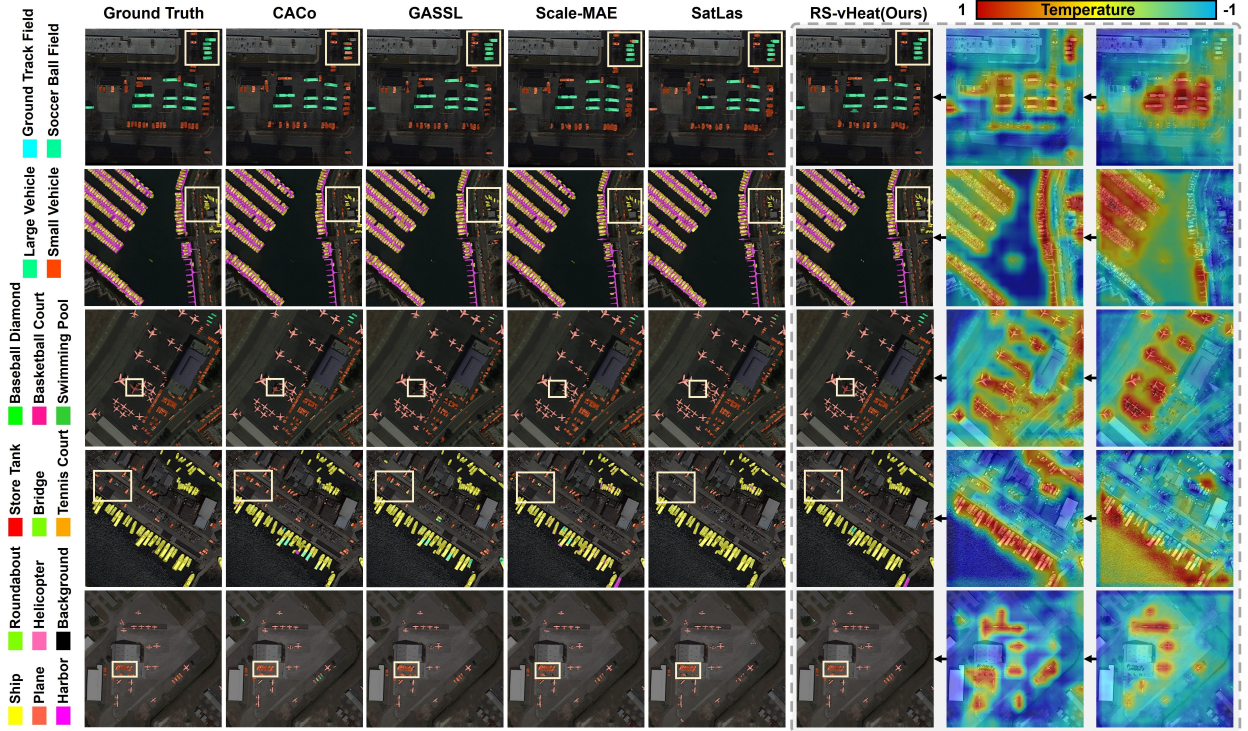


Figure 7: The qualitative results of RS-vHeat and several representative RSFMs on the iSAID dataset. Each column from left to right represents: ground truth, CACo (ResNet-18), GASSL (ResNet-50), Scale-MAE (ViT-L), Satlas (Swin-B), and the results from our model, RS-vHeat. The last two columns on the right visualize the output variations of RS-vHeat across the final two stages.

Table 10: Comparison of AP_{50} for each category, mAP_{50} and mAP_{75} on SAR-AIRcraft-1.0 with other specialized models.

Method	Publication	A330	A320/A321	A220	ARJ21	Boeing737	Boeing787	Other	$mAP_{50} \uparrow$	$mAP_{75} \uparrow$
Faster R-CNN Ren et al. [2016]	TPAMI'2016	85.0	97.2	78.5	74.0	55.1	72.9	70.1	76.1	62.2
Cascade R-CNN Cai and Vasconcelos [2018]	CVPR'2018	87.4	97.5	74.0	78.0	54.5	68.3	69.1	75.7	58.9
RepPoints Yang et al. [2019]	ICCV'2019	89.8	97.9	71.4	73.0	55.7	51.8	68.4	72.6	53.3
SKG-Net Fu et al. [2021]	JSTARS'2021	79.3	78.2	66.4	65.0	65.1	69.6	71.4	70.7	46.4
SA-Net Zhirui et al. [2023]	RADARS'2023	88.6	94.3	80.3	78.6	59.7	70.8	71.3	77.7	62.8
RS-vHeat (Ours)	-	98.4	97.9	81.1	89.3	82.0	79.8	81.1	87.1	67.4

D.1. Single- and multi-modal semantic segmentation

We utilize RS-vHeat as the visual encoder and implemented UPerNet Xiao et al. [2018] with cross-entropy loss for the output head. Additionally, we employ the AdamW optimizer with a learning rate of $6e-5$ and conduct a warm-up of 1500 iterations.

Dataset. We evaluated our model on three single-modal datasets and one multi-modal dataset:

- 1) The Potsdam dataset Sherrah [2016] comprises 38 images. This dataset is annotated with six classes, each having a resolution of 6000×6000 pixels. The input resolution is set to 512 pixels.
- 2) The iSAID dataset Waqas Zamir et al. [2019] comprises 2,806 images with varying resolutions, primarily focusing on urban environments. The dataset includes annotations for 15 different categories and we utilize an image size of 896 pixels as the input for the model.

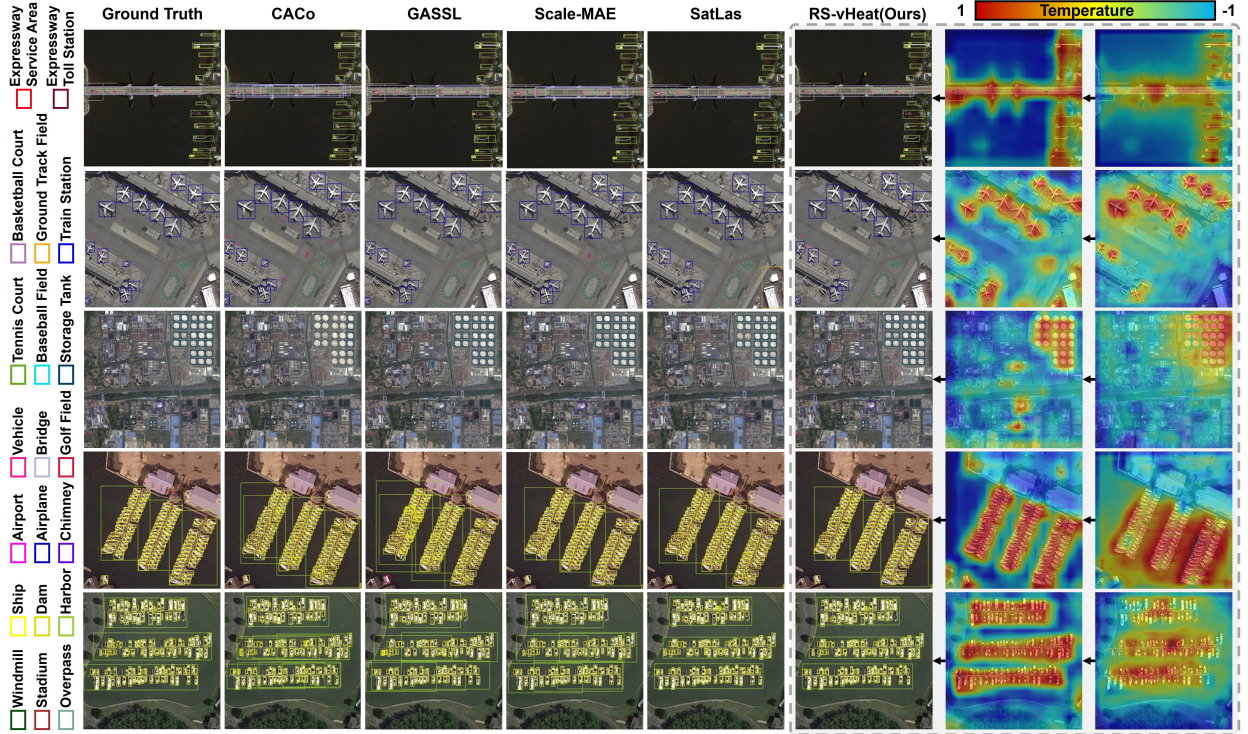


Figure 8: The qualitative results of RS-vHeat and several representative RSFMs on the DIOR dataset. Each column from left to right represents: ground truth, CACo (ResNet-18), GASSL (ResNet-50), Scale-MAE (ViT-L), Satlas (Swin-B), and the results from our model, RS-vHeat. The last two columns on the right visualize the output variations of RS-vHeat across the final two stages.

3) The Air-PolSAR-Seg dataset Wang et al. [2022b] focuses on polarimetric SAR images. It offers a region measuring 9082×9805 pixels and includes 2,000 image patches, each sized 512×512 . The dataset features pixel-wise annotations covering six categories. We adopt a size of 512 pixels for the image input.

4) The WHU-OPT-SAR dataset Li et al. [2022] is a multi-modal segmentation dataset with a resolution of 5 meters. It includes optical and SAR data from the same region, categorized into seven classes. Each image has a size of 5556×3704 pixels. We uniformly cropped the multi-modal images to a pixel size of 256 for model input.

Metric. Following the configurations of RingMo Sun et al. [2022b] and SkySense Guo et al. [2024], we evaluate the mean Intersection over Union (mIoU) on the iSAID dataset and test the mean F1 score (mF1) on the Potsdam dataset. For the AIR-PolSAR-Seg dataset, we use three metrics: mIoU, Overall Accuracy (OA) and Average Accuracy (AA). We assess OA and User’s Accuracy on the WHU-OPT-SAR dataset following the setup outlined in the corresponding paper.

Additional Results. The fig. 7 displays the process visualizations and prediction results for the iSAID dataset, which display that the heat-conduction-based backbone exhibits adaptive characteristics when capturing features across different layers.

D.2. Object Detection

We conduct coarse- and fine-grained experiments on optical and SAR datasets to demonstrate the robustness of RS-vHeat. In the horizontal bounding boxes (HBB) task, we employ SGD as the optimizer, with a base learning rate set to 0.01. A warm-up phase of 3 epochs is conducted. YOLOX Ge et al. [2021] is used as the output head, and experiments are conducted using cross-entropy loss and IoU loss. In the oriented bounding box (OBB) task, we adjust the base learning rate to $1e-4$. The warm-up phase consists of 500 iterations. Oriented RCNN Xie et al. [2021c] is used as the output head, applying cross-entropy and Smooth \mathcal{L}_1 loss.

Dataset. Our model is tested on three challenging object detection datasets:

1) FAIR1M Sun et al. [2022a] is an optical fine-grained dataset with objects annotated using OBB, encompassing five major categories, further divided into 37 subcategories. The dataset contains over 40,000 images. Following the official

split, we ultimately submitted the test results to the website to obtain accuracy measurements. We utilize an image size of 512 pixels as the input for the model.

2) SAR-AIRcraft-1.0 Zhirui et al. [2023] is a HBB fine-grained SAR aircraft object detection dataset designed for challenging scenarios, totaling 4,368 images. It encompasses seven fine-grained categories. We adopt a size of 640 pixels for the image input.

3) DIOR Li et al. [2020a] is an optical dataset that includes 20 categories. It comprises a total of 23,463 images and provides HBB annotations. We utilize an image size of 800 pixels as the input for the model.

Metric. On the FAIR1M and DIOR dataset, we evaluate the mAP (Mean Average Precision). For the SAR-AIRcraft-1.0 dataset, we evaluate the AP_{50} for each category, mAP_{50} and mAP_{75} . mAP_{50} and mAP_{75} represent the mAP at IoU thresholds of 0.5 and 0.75, respectively, with category-specific precision calculated at an IoU threshold of 0.5.

Additional Results. The visualization results of the DIOR dataset are shown in fig. 8. From the feature extraction process and results, RS-vHeat outperforms other RSFMs in terms of extracting dense RS objects. Additionally, we further refine the RS-vHeat extraction results for each class of the SAR-AIRcraft-1.0 dataset in table 10, highlighting its enhanced capability in recognizing various aircraft types in SAR scenarios compared to specialized object detection models.

D.3. Change Detection

We employ RS-vHeat as the visual encoder, accommodating images before and after transformation. AdamW optimizer is used with a base learning rate of 0.002 and we train for 200 epochs. The BIT architecture Chen et al. [2021] is utilized for subsequent image change analysis, with cross-entropy loss applied for the experiments.

Dataset. We use the LEVIR-CD dataset to train and test:

1) The LEVIR-CD dataset Chen and Shi [2020] consists of 637 image patch pairs obtained from Google Earth. Each patch has a size of 1024×1024 pixels. The dataset primary focus is on building-related changes, such as the emergence of new structures and the decline of existing ones. We utilize an image size of 256 pixels as the input.

Metric. We use F1-score to evaluate change detection performance. F1-score is the harmonic mean of precision and recall, providing a balanced measure of performance.

D.4. Image Classification

We extend our model by attaching a classification head designed to handle the classification task and employ cross-entropy loss for computation. We utilize AdamW as the optimizer with a learning rate of $5e-4$, training for 300 epochs.

Dataset. We validate our model on two benchmark datasets as described below.

1) The Aerial Image Dataset (AID) Xia et al. [2017] consists of 30 categories, with each category containing approximately 220 to 420 images sized at 600×600 pixels, totaling 10,000 images.

2) The NWPU-RESISC45 dataset Cheng et al. [2017] is a RS image dataset comprising 45 categories, with a total of 31,500 images distributed across these categories. Each category consists of 700 images.

Metric. We use OA to evaluate classification performance. We follows standard practices in the field Guo et al. [2024], using 20% and 50% of the AID dataset as training sets, and 10% and 20% of the NWPU-RESISC45 dataset as training sets.